J Adv Ceram

Research Article

Optimizing magnetic and electrical properties of MnZn ferrites via spatially engineered Ni distribution

Tao Wu[1], Chaoming Wang[2], Zenan Ma[1], Zhenyu He[2], Xiaofeng Zhang[1], Zhongwen Lan[1], Zhong Yu[1], Xiaona Jiang[1], Qifan Li[1], Chuanjian Wu[1,✉], Ke Sun[1,✉]

Cite this article: Wu T, Wang C, Ma Z, et al. *J Adv Ceram* 2026, **15**(2): 9221240. https://doi.org/10.26599/JAC.2026.9221240

ABSTRACT: Manganese-zinc (MnZn) ferrites are widely employed in electromagnetic interference (EMI) suppression due to their favorable magnetic properties. However, their practical performance is often constrained by the inherent trade-offs among key magnetic properties, such as initial permeability (μ_i), standardized impedance (Z_0), saturation magnetic induction (B_s), and Curie temperature (T_c). Here, we demonstrate a strategy that simultaneously enhances these properties by combining trace Ni doping with precise control of the sintering atmosphere. The low Ni concentration, together with a carefully regulated oxygen partial pressure, suppresses the diffusion driving force of Ni^{2+}, leading to its spatially nonuniform distribution and preferential segregation at grain boundaries. This localized Ni enrichment facilitates the formation of transgranular magnetic domains across significant crystallographic misorientation grains. Furthermore, Ni-rich grain boundaries promote the migration of Fe^{3+} from octahedral (B) sites to tetrahedral (A) sites, thereby increasing the A–B and A–A bond angles, shortening the corresponding bond lengths, and strengthening the superexchange interactions within the spinel lattice. As a result of this spatially engineered Ni distribution, the optimized MnZn ferrite exhibits significantly improved properties, including a μ_i of 11,648 at 10 kHz, Z_0 of 43 Ω·mm^{-1} at 1 MHz, B_s of 524 mT at 1 kHz, 1194 A·m^{-1}, and T_c of 174 °C, outperforming conventional MnZn ferrites. This work highlights spatial compositional engineering as a viable route to advanced soft magnetic materials for next-generation EMI suppression technologies.

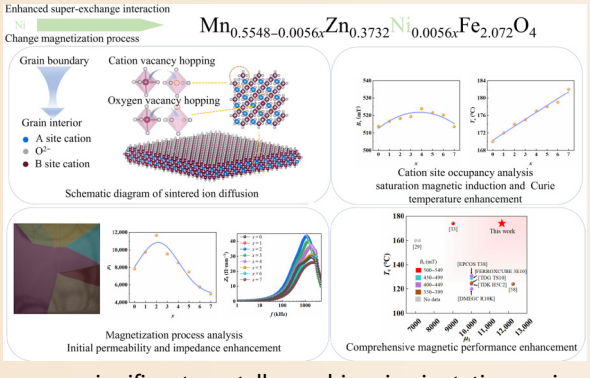

KEYWORDS: manganese-zinc (MnZn) ferrites; Ni distribution; magnetic domains; superexchange interaction

1 Introduction

The rapid advancement of modern electronic systems has led to increasingly severe harmonic pollution in power grids and electronic circuits, posing significant risks to the stability and reliability of critical components [1–4]. While high-frequency electromagnetic interference (EMI) has long been the primary concern in communication circuits, low-to-mid frequency EMI (kHz to MHz), mainly originating from switched mode power converters, is equally critical for the reliable operation of power electronic devices. In response to this evolving technological landscape, there is an urgent demand for high-performance magnetic core materials that can simultaneously deliver high initial permeability (μ_i), impedance (Z), saturation magnetic induction (B_s), and Curie temperature (T_c). These properties directly determine the current-handling capacity, operating frequency range, filtering performance, and thermal stability of EMI filters. Among various soft magnetic materials, manganese–zinc (MnZn) ferrites are particularly attractive for EMI suppression in the kHz-MHz frequency range due to their intrinsically high μ_i and B_s [5–9]. Consequently, they have been widely employed in data center power supplies, electric vehicles, renewable energy converters, and base station power modules [10,11]. However, in MnZn ferrites, μ_i, Z, B_s, and T_c are governed by distinct yet strongly coupled magnetic mechanisms, making their simultaneous optimization inherently challenging. Enhancing one parameter usually requires microstructural or electronic modifications that inevitably compromise others. Specifically, achieving high μ_i relies on large grain sizes, low magnetocrystalline anisotropy (K_1), and a high density of mobile domain walls. Such microstructural features, however, shift the domain wall and spin rotation relaxation processes toward lower frequencies, thereby deteriorating the high-frequency Z. In contrast, increasing B_s and T_c requires strengthening the A–B superexchange interaction, typically by increasing the Fe^{3+}/Fe^{2+} ratio or reducing the Zn^{2+} content. These compositional

[1] School of Materials and Energy, University of Electronic Science and Technology of China, Chengdu 610054, China. [2] Hengdian Group DMEGC Magnetics Company Limited, Dongyang 322100, China.

✉ Corresponding authors. E-mail: C. Wu, wcjuestc2005@uestc.edu.cn; K. Sun, ksun@uestc.edu.cn

Received: November 6, 2025; Revised: December 19, 2025; Accepted: January 5, 2026

adjustments simultaneously increase K_1 and suppress domain wall mobility, leading to a reduction in μ_i. As a result, the fundamental physical requirements for maximizing μ_i, Z, B_s, and T_c are intrinsically conflicting, rendering their concurrent enhancement in MnZn ferrites extremely difficult.

To address this challenge and improve the comprehensive magnetic performance of MnZn ferrites, two main strategies have been extensively explored. The first involves the incorporation of various additives to optimize the microstructure and grain boundary characteristics. For instance, fluxing additives can enhance cation diffusion by forming transient liquid phases during sintering, thereby promoting grain growth and structural densification [12–16]. Li *et al.* [17] systematically investigated the effects of Sb_2O_3 additives on the magnetoelectric properties of MnZn ferrites. During high-temperature sintering, Sb_2O_3 forms a transient liquid phase at grain boundaries, generating capillary forces that facilitate particle rearrangement, sliding, and mass transport. These effects enhance particle coalescence and grain growth, resulting in an increased average grain size and thinner grain boundaries. Consequently, the grain boundary pinning effect is significantly reduced, enabling more facile domain wall motion and leading to an enhanced μ_i (3493). Additionally, liquid phase-assisted densification increases the magnetic moment density, contributing to an elevated B_s (534 mT). The segregation of Sb_2O_3 at grain boundaries also improves the resistivity (12 Ω·m), further benefiting the overall magnetoelectric performance. However, these enhancements exhibit a strong concentration dependence, with optimal properties achieved at a doping level of 0.01 wt%. Beyond this threshold, the formation of detrimental secondary phases impairs both magnetic and electrical performance. Ying *et al.* [18] examined the influence of MoO_3 as a fluxing agent on the magnetic properties of MnZn ferrites. The presence of liquid-phase MoO_3 at grain boundaries promoted grain growth and improved microstructural uniformity and densification, yielding increases in both μ_i (5950) and B_s (526 mT). The Z spectroscopy confirmed that MoO_3 primarily acts at grain boundaries, contributing to improved Z. However, the enhancement in T_c was limited. In contrast, high-resistivity additives [19–23] primarily modify grain boundary composition to enhance resistivity. Andalib *et al.* [24] proposed a strategy involving the incorporation of insulating magnetic inclusions at grain boundaries. The accumulation of high-resistivity phases significantly increased the grain boundary resistance (up to 20 kΩ), thereby enhancing the overall Z. Although the introduced ferrimagnetic $Y_3Fe_5O_{12}$ (YIG) nanoparticles possess relatively low μ_i, their capacity for sustaining long-range magnetic interactions remains largely intact. Nonetheless, the inclusion of YIG led to a reduction in μ_i due to the disruption of continuous magnetic pathways and dilution of high μ_i phases. Töpfer *et al.* [25] synthesized MnZn ferrite composite additives via chemical methods and investigated the effects of SnO_2 incorporation. SnO_2 significantly improved the resistivity by forming insulating grain boundary phases and suppressing the Fe^{3+} concentration, thereby limiting electron hopping conduction. At the same time, SnO_2 acted as a sintering aid, promoting grain growth and increasing bulk density, which moderately enhanced B_s. However, a reduction in μ_i from 2000 to 1700 was observed, attributed to the altered temperature dependence of μ_i and modified magnetic anisotropy caused by SnO_2. Although additive engineering can significantly improve certain properties, its influence on T_c remains limited, as T_c is predominantly governed by the material's fundamental composition and the strength of superexchange interactions.

The second major strategy focuses on tuning the intrinsic lattice structure through ion substitution. This approach can affect lattice constants [26–28], magnetic anisotropy constants [29,30], net magnetic moment per unit cell [31,32], and superexchange interactions [33,34]. For example, Zipare *et al.* [35] investigated Dy-substituted MnZn ferrites and found that Dy^{3+} ions preferentially occupy octahedral (B) sites in the spinel lattice, leading to an increase in the lattice constant. However, both B_s and T_c exhibited a decline with increasing Dy substitution, which can be attributed to a reduction in the net magnetic moment per formula unit. Jeong *et al.* [36] examined MnZn ferrites with varying Ni substitution levels. Increasing Ni substitution resulted in decreased lattice constants (8.52 Å), μ_i (1100), and ρ (24 Ω·cm) while simultaneously improving density (4.67 g·cm^{-3}) and T_c (250 °C). Similarly, Ahmed *et al.* [37] reported that Ni substitution reduced the lattice constant (8.39 Å), μ_i, and coercivity (20 Oe) but led to an increase in the specific saturation magnetization (34.2 emu·g^{-1}), and the magnetic anisotropy constant increased progressively. Despite these advances, the strong intrinsic coupling among multiple magnetic parameters continues to hinder their simultaneous optimization at a high overall performance level. Moreover, most studies on Ni substitution have focused on relatively high doping concentrations. Recent work suggests that even trace dopants, when enriched at grain boundaries, can markedly alter the magnetization behavior of MnZn ferrites [38,39]. However, the mechanisms through which grain boundary-enriched Ni influences magnetic coupling and magnetization processes remain poorly understood. This knowledge gap is particularly critical for EMI filter applications, where each magnetic parameter directly affects device performance and operational stability.

In this study, we propose a strategy to enhance the overall magnetic performance of MnZn ferrites, including μ_i, Z, B_s, and T_c, by regulating the spatial distribution of Ni ions. Through trace Ni doping and precise control of oxygen partial pressure during sintering, the diffusion of Ni^{2+} is strategically modulated to achieve enrichment at grain boundaries. This spatially nonuniform distribution strengthens intergranular magnetic coupling, facilitating the formation of transgranular magnetic domains and thereby improving μ_i and Z. Concurrently, the preferential occupation of Ni^{2+} at B sites drives Fe^{3+} migration to tetrahedral (A) sites, enhancing A–B and A–A superexchange interactions and leading to increased T_c. The Ni-induced modulation of magnetic moments and microstructure also contributes to an elevated B_s. The synergistic effects of these mechanisms significantly boost the comprehensive magnetic performance of MnZn ferrites, offering considerable potential for next-generation EMI suppression applications.

2 Experimental

2.1 Synthesis

Ni-substituted MnZn ferrites were synthesized via a conventional solid-state reaction method, with the target chemical formula $Mn_{0.5548-0.0056x}Zn_{0.3732}Ni_{0.0056x}Fe_{2.072}O_4$, where x ranges from 0 to 7. The corresponding stoichiometric ratios of the raw materials were 19 mol% ZnO, 52.75 mol% Fe_2O_3, 28.25–26.25 mol% MnO, and 0–2 mol% NiO, depending on the desired substitution level. The raw powders were first mixed with deionized water and milled in a planetary ball mill for 1 h using a ball-to-powder-to-water mass ratio of 3 : 1 : 1.5. The resulting slurry was dried and subsequently presintered at 850 °C for 2 h to promote solid-state diffusion and phase formation. The presintered powders were then blended with selected additives and subjected to a second ball milling step

for 2 h to ensure homogeneity. After drying, the powders were granulated with 12 wt% polyvinyl alcohol (PVA) as a binder and compacted into toroidal cores using a uniaxial pressing method. Finally, the samples were sintered at 1360 °C for 6 h in a tube furnace (GSL 14-1, Hunan Jinlu Intelligent Manufacturing Co., Ltd., China). The sintering process consisted of an initial air atmosphere stage followed by a nitrogen atmosphere stage. Throughout the process, the oxygen partial pressure was precisely regulated using mass flow controllers and a closed-loop feedback system, ensuring effective densification and microstructural development.

2.2 Characterization

The surface morphology and elemental distribution were examined using a scanning electron microscope (SEM; Apreo 2, Thermo Scientific, USA). Detailed analyses of the microstructure, composition, and magnetic domain features were further performed using a transmission electron microscope (TEM; F200X, Talos, USA). The site occupancy of Fe ions was examined at room temperature using a spectroscope (Mössbauer; MR-2500, Wissel, Germany) with a ^{57}Co radioactive source. The velocity scale was calibrated against an α-Fe foil at room temperature. Therefore, all isomer shifts (IS) reported in this work are given relative to α-Fe. Surface vibrational modes were identified through a Raman spectroscope (Horiba LabRAM HR Evolution, Japan) using a 532 nm laser at 2 mW power, while chemical states were analyzed using an X-ray photoelectron spectroscope (XPS; K-Alpha, Thermo Scientific, USA). The phase structure of the samples was characterized by X-ray diffraction (XRD) using a PANalytical Aeris Benchtop diffractometer (UK). Elemental composition was determined via inductively coupled plasma-optical emission spectrometer (ICP-OES; Avio 550 Max, PerkinElmer, USA). *Z* characteristics, inductance, and resistivity were evaluated using an inductance, capacitance, and resistance (LCR) meter (Tonghui 2826, China). B_s was determined with a *B-H* analyzer (SY8218, IWATSU, Japan).

3 Results and discussion

3.1 Elemental distribution and magnetization process

As shown in Fig. 1(a), stoichiometric mixtures of Fe_2O_3, Mn_3O_4, NiO, and ZnO were presintered to promote solid-state reactions, followed by secondary milling to refine the powders and enhance homogeneity. Final sintering was conducted under a controlled atmosphere with elevated oxygen partial pressure to regulate elemental diffusion and promote densification.

The design principle is schematically illustrated in Fig. 1(b) from the perspective of defect chemistry and diffusion dynamics. In MnZn ferrites, the type, concentration, and spatial distribution of point defects are predominantly controlled by the oxygen

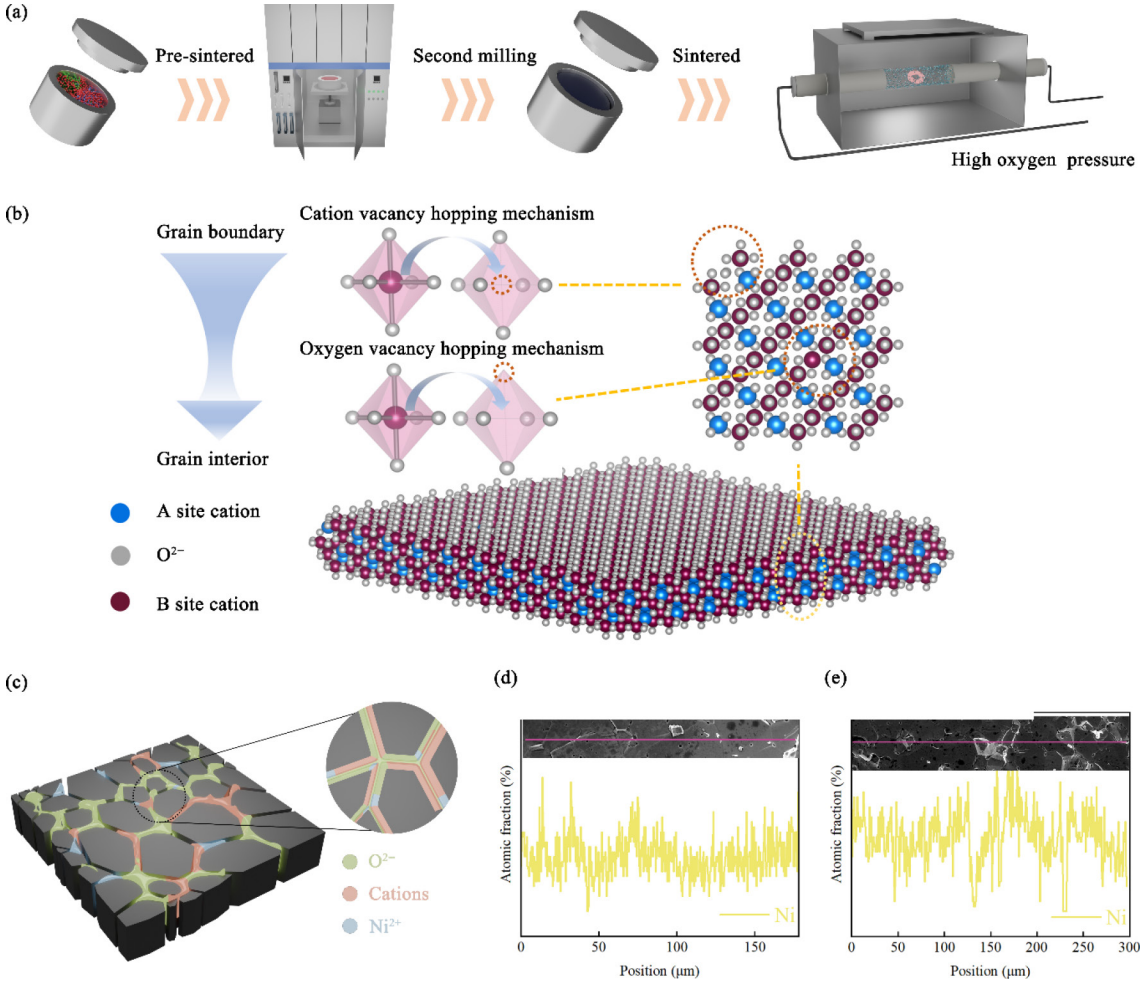

Fig. 1 Influence of sintering atmosphere and formula on the composition distribution of MnZn ferrite: (a) flowchart of sample preparation, (b) schematic illustration of ion diffusion and chemical potential evolution during MnZn ferrite sintering, (c) schematic diagram of macroscopic ion distribution of MnZn ferrite, (d) composition distribution of sintering curve 1, and (e) composition distribution of sintering curve 2.

partial pressure [40], which consequently dictates the diffusion pathways and the ultimate distribution of Ni between grain interiors and grain boundaries. Under high oxygen partial pressure, the formation of oxygen vacancies is strongly suppressed. In this regime, cation diffusion proceeds primarily via vacancy-assisted hopping and transport along grain boundaries. Given their higher free energy and greater density of cation vacancies, grain boundaries offer energetically favorable pathways with reduced migration barriers. Thus, they become the preferred diffusion channels, leading to partial segregation and local enrichment of Ni^{2+} at the boundaries. In contrast, under low oxygen partial pressure, the reducing atmosphere promotes a significant increase in the concentration of oxygen vacancies. These vacancies are not confined to grain boundaries but are widely distributed throughout the grain interior, thereby enhancing bulk diffusion. For Ni^{2+} ions with a fixed valence state, the formation of transient vacancy cation complexes further lowers the activation energy for migration, allowing Ni to diffuse more uniformly into the lattice and yielding a homogeneous intragranular distribution. Figure 1(c) summarizes the resulting macroscopic Ni distribution under high oxygen partial pressure.

In this work, the oxygen partial pressure was precisely modulated throughout the sintering process. During the intermediate stage (800–1200 °C), a strongly reducing atmosphere was applied to maintain Mn in the divalent state. The oxygen partial pressure was then increased during the isothermal holding stage and rapidly reduced prior to cooling. This sequence prevented undesirable Mn valence variations while driving Ni^{2+} segregation toward the grain boundaries. To quantitatively assess the extent of segregation, elemental mapping was performed on samples corresponding to sintering curves 1 and 2 (Fig. S1 in the Electronic Supplementary Material (ESM)).

As shown in Fig. 1(d), distinct Ni enrichment was detected along approximately half of the grain boundaries under high-oxygen sintering, whereas this feature disappeared under low-oxygen conditions (Fig. 1(e)). Therefore, precise oxygen control effectively governs Ni^{2+} mobility. Higher oxygen partial pressure suppresses cation diffusion and results in a nonuniform, boundary-enriched Ni distribution within the ceramic matrix.

High-resolution transmission electron microscopy (HRTEM) was further employed to analyze the crystal structure and compositional features. The sample selected for this analysis corresponds to the $x = 2$ composition, and a representative image is shown in Fig. 2(a). Figures 2(b)–2(g) display the HRTEM images and corresponding fast Fourier transform (FFT) patterns for grains G1, G2, and G3. For the G1 grain, lattice spacings of 1.92 and 2.57 Å were identified, corresponding to the $(\bar{3}13)$ and (311) planes along the $[2\bar{3}\bar{3}]$ zone axis. In contrast, the G2 grains show lattice spacings of 3.00 and 4.91 Å, assigned to the (220) and $(1\bar{1}1)$ planes along the $[\bar{1}1\bar{2}]$ zone axis. Similarly, the G3 grains exhibit lattice spacings of 3.03 and 4.92 Å, attributed to the $(1\bar{1}1)$ and (202) planes along the $[10\bar{1}]$ zone axis. These observations confirm distinct crystallographic orientations and notable misorientations among the grains, which play a critical role in determining magnetic domain wall behavior at grain boundaries.

Elemental distributions across grain boundaries were analyzed, as shown in Figs. 2(h)–2(o). In region A1 (corresponding to the G1/G3 interface), the concentrations of most elements remained relatively uniform, except for a distinct enrichment of Ni at the grain boundary. In contrast, regions A2 and A3 (representing the G1/G2 and G2/G3 interfaces) have homogeneous elemental distributions without noticeable Ni segregation (Fig. S2 in the ESM). This localized Ni enrichment at the G1/G3 boundary may facilitate magnetic coupling despite the high misorientation angle.

In situ Lorentz transmission electron microscopy (LTEM) observations further confirm the crucial role of Ni in domain wall dynamics. Figure 3(a) presents LTEM observations of a MnZn ferrite sample with a Ni substitution level of $x = 2$ under an applied magnetic field. Clear cross-grain magnetic domains are observed in both underfocused and overfocused LTEM images, indicating coherent magnetization across grain boundaries. Figures 3(b)–3(j) depict the dynamic evolution of magnetic domain walls under varying external magnetic fields, with distinct colors representing different domain orientations. As the field strength increases or decreases, domain regions expand or contract accordingly, demonstrating a reversible domain wall motion. Domains aligned with the field direction preferentially grow by assimilating neighboring misaligned domains, reflecting field-driven domain coalescence and magnetic realignment.

Magnetic exchange coupling across grain boundaries can promote the magnetization of adjacent grains [39]. However, significant crystallographic misorientation between neighboring grains can suppress intergranular exchange interactions, thereby impeding the formation of continuous magnetic domains. In the present study, the misorientation angles between grains G1/G2, G2/G3, and G1/G3 are measured to be 16.8°, 30.0°, and 41.1°, respectively. Due to the relatively small angle at the G1/G2 boundary, transgranular domains are observed even under low magnetic fields, indicating effective intergranular magnetic coupling. In contrast, the G2/G3 boundary, with its large misorientation, consistently obstructed domain wall propagation, even at elevated fields. Interestingly, despite the similarly large misorientation at the G1/G3 boundary, transgranular domain formation was still observed under higher magnetic fields, implying the presence of additional influencing factors beyond crystallographic alignment. Based on the HRTEM results, in region A1 (corresponding to the G1/G3 interface), the concentrations of most elements remained relatively uniform, except for a distinct enrichment of Ni at the grain boundary. In contrast, regions A2 and A3 (representing the G1/G2 and G2/G3 interfaces) have homogeneous elemental distributions without noticeable Ni segregation (Fig. S2 in the ESM). This localized Ni enrichment at the G1/G3 boundary may facilitate magnetic coupling despite the high misorientation angle, offering a plausible explanation for the observed transgranular domain behavior. A full sequence of LTEM images under varying magnetic field conditions is provided in Fig. S3 in the ESM, and the complete domain evolution process is documented in the supplementary video (Fig. S4 in the ESM).

3.2 Site occupancy and superexchange interaction

To elucidate the site occupancy and its impact on the magnetic behavior of MnZn ferrites, a comprehensive suite of characterization techniques was employed, including Mössbauer spectroscopy (MS), Raman spectroscopy, X-ray diffraction (XRD), and XPS, as presented in Figs. 4, S5–S7, and Table S1 in the ESM.

In conventional MnZn ferrites, the Mössbauer spectrum typically consists of two magnetic sextets corresponding to Fe ions located at the A and B sites, along with a paramagnetic doublet, as shown in Figs. 4(a) and 4(b). The corresponding fitted parameters, such as IS, quadrupole splitting (QS), hyperfine field (H) and relative area (R_A) [41–44], are summarized in Table S2 in the ESM. The observed IS values of 0.37 mm·s^{-1} for A sites and 0.45 mm·s^{-1} for B sites confirm the presence of Fe ions in both crystallographic environments. The higher IS value at the B site reflects stronger crystal field stabilization, attributed to the higher coordination number and shorter Fe–O bond lengths. As Ni

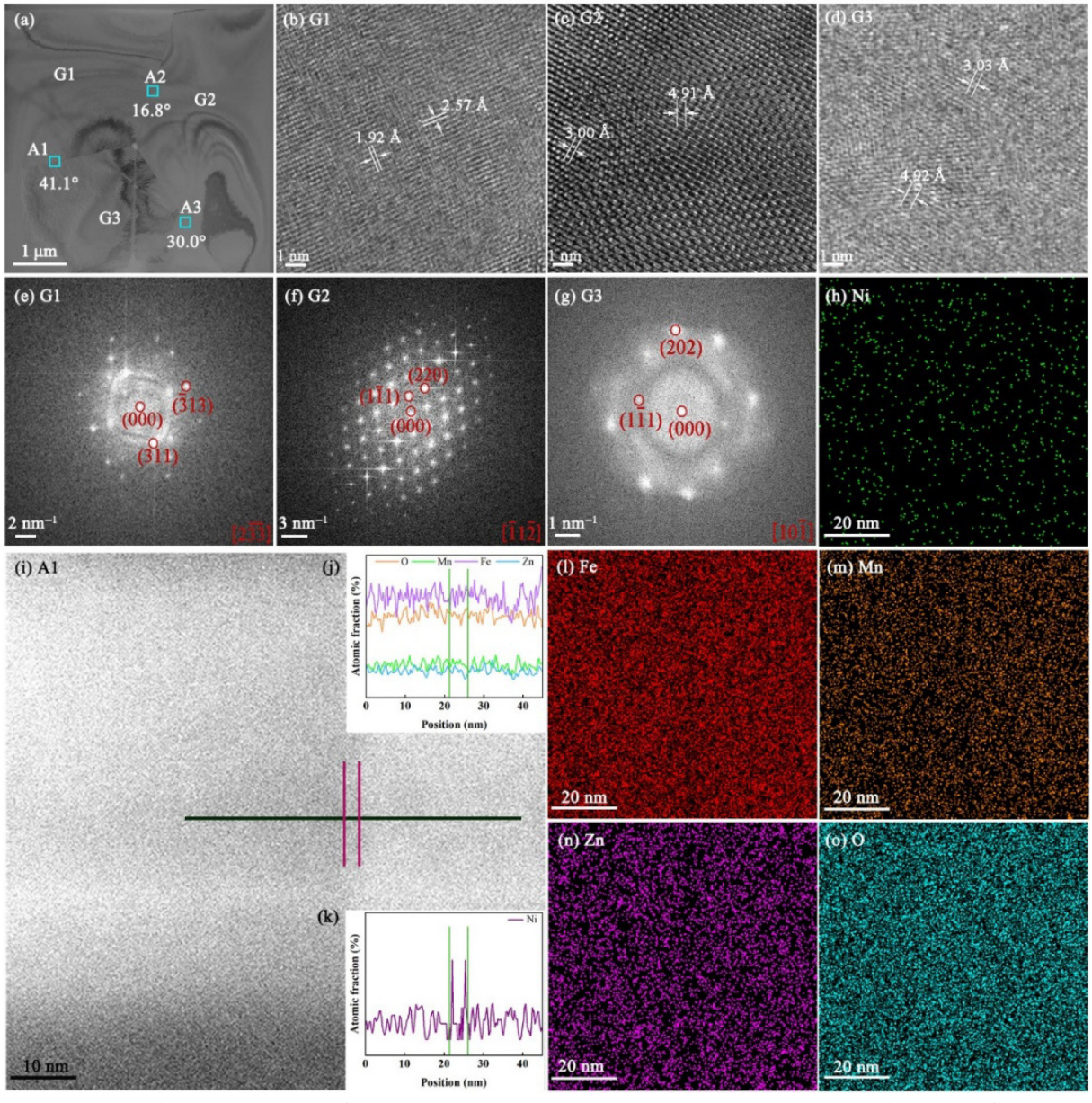

Fig. 2 Crystal structure and elemental distribution of Ni-substituted MnZn ferrite (x = 2). (a) TEM image; (b–g) HRTEM and FFT images for G1, G2, and G3; (h–o) High-angle annular dark field (HADDF) and energy dispersive spectroscopy (EDS) elemental mappings images for A1.

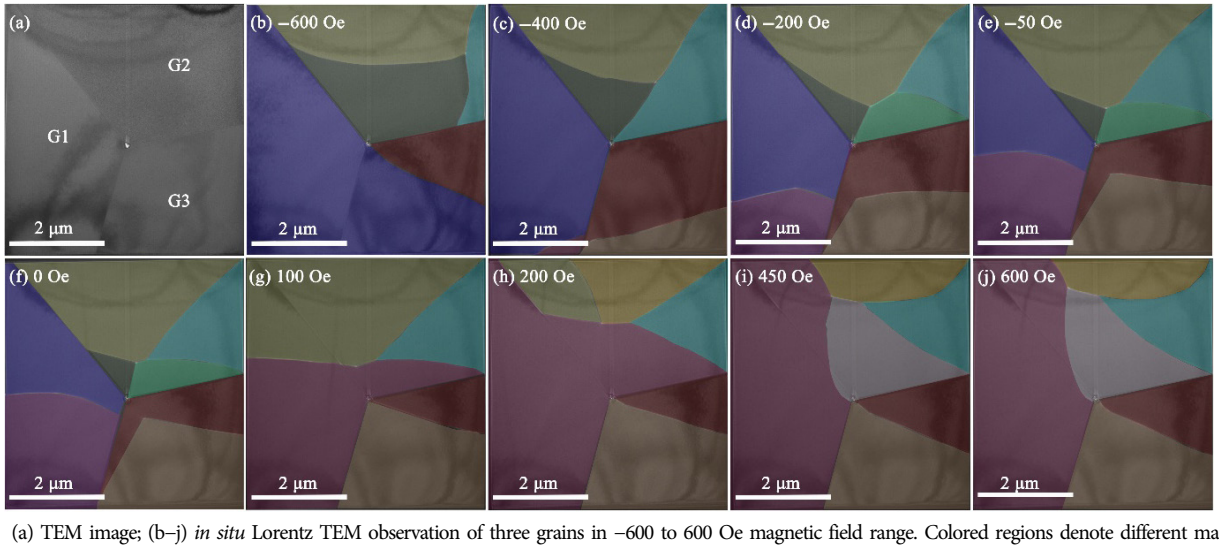

Fig. 3 (a) TEM image; (b–j) *in situ* Lorentz TEM observation of three grains in −600 to 600 Oe magnetic field range. Colored regions denote different magnetic domains.

substitution does not alter the nuclear charge of Fe ions, the IS remains relatively unaffected by Ni substitution. In contrast, QS shows a clear increasing trend with increasing Ni substitution, indicating a reduction in local symmetry and an enhanced electric field gradient (EFG) at the Fe nucleus. This observation is consistent with the preferential occupation of B sites by Ni^{2+} ions, which induces local lattice distortions and increases asymmetry in the electron distribution. The hyperfine magnetic fields measured at the A and B sites (41 and 35 T, respectively) are consistent with previously reported values for MnZn ferrites [45]. Notably, the H strength increases with increasing Ni substitution, suggesting enhanced superexchange interactions, a conclusion further supported by subsequent analyses of Fe–O–Fe bond angles and cation redistribution. The R_A analysis reveals a gradual increase in Fe^{3+} occupancy at the A site and a corresponding decrease at the B site with increasing Ni substitution, indicating the migration of Fe^{3+} cations from B to A sites. Although a small fraction of Fe^{2+} ions is expected to remain at the B site, their concentration is too low to yield a distinct Mössbauer signature [46].

Raman spectroscopy provides complementary insights into local cation environments in spinel ferrites by analyzing vibrational modes. In the Raman spectra, the A_{1g} mode corresponds to the symmetric stretching of metal–oxygen (M–O) bonds at the A sites [47,48]. As shown in Figs. 4(c) and 4(d), the A_{1g} peak exhibits a systematic blueshift with increasing Ni substitution, indicating a strengthening of the M–O bonds. This shift is primarily attributed to the smaller ionic radius and higher field strength of Ni^{2+} relative to Mn^{2+}, resulting in stiffer Ni–O bonds and increased vibrational force constants. Additionally, quantitative analysis of the fitted peak areas reveals a decrease in Mn^{2+} content and a corresponding increase in Fe^{3+} occupancy at the A sites, providing further evidence for Ni-induced cation redistribution. The detailed Raman peak positions of all samples are summarized in Table S3 in the ESM.

Rietveld refinement of the XRD patterns, as shown in Figs. 4(e) and 4(f), confirms the formation of a single-phase spinel structure (JCPDS No. 74-2401) across all compositions. The high quality of the refinement is evidenced by the low reliability factors, with the refined fitting parameters (R_{wp} and R_p) values below 3%, indicating excellent agreement between the experimental data and the fitted model. Table S4 in the ESM presents R_{wp}, R_p, cation distribution, and lattice constants obtained for MnZn ferrite. The elemental compositions determined by ICP-OES (Table S5 in the ESM) show that the deviations are nearly all below 2%, while the consistency of the cation occupancy results obtained from multiple methods (Table S6 in the ESM) further validates the reliability of the structural analysis. The schematic illustration in Fig. 4(g) depicts the proposed site occupancy mechanism: Ni^{2+} preferentially occupies B sites, displacing Fe^{3+} to A sites and promoting Mn^{2+} migration into both the A and B sublattices. As expected, Zn^{2+} predominantly resides at A sites, while Fe^{2+} and Ni^{2+} exhibit a strong preference for B site occupancy. Mn^{2+} is distributed across both sublattices, with an approximate A : B site ratio of 4 : 1, consistent with previous reports [49,50]. Notably, the lattice constant decreases with increasing Ni substitution, which is attributed to the substitution of larger Mn^{2+} (0.82 Å) [51] by smaller Ni^{2+} (0.69 Å) [52], resulting in a contraction of the unit cell.

Based on the established site occupancy data, the average ionic radii at sites A and B (r_a and r_b) were calculated according to Eqs. (1) and (2) [53]. As shown in Fig. 5(a), r_a decreases progressively with increasing Ni substitution, which is attributed to the migration of smaller Fe^{3+} (0.67 Å) [54] into the A sites. In contrast, r_b remains nearly unchanged, suggesting a compensation effect between the incorporation of smaller Ni^{2+} and the simultaneous reduction of larger Mn^{2+} at the B sites. Furthermore, the theoretical lattice constants (a_{th}), derived from Eq. (3) [50] based on the calculated ionic radii and site occupancy, show excellent agreement with the experimentally measured values, as illustrated in Fig. 5(b). This consistency further validates the reliability of the proposed site occupancy model (Eqs. (1)–(3)):

$$r_a = (m_{Mn^{2+}} \times 0.82 + m_{Zn^{2+}} \times 0.82 + m_{Fe^{3+}} \times 0.67) \quad (1)$$

$$r_b = 0.5 \times (m_{Mn^{2+}} \times 0.82 + m_{Ni^{2+}} \times 0.72 + m_{Fe^{2+}} \times 0.74 + m_{Fe^{3+}} \times 0.67) \quad (2)$$

$$a_{th} = \frac{8}{3\sqrt{3}}[r_a + R_o + \sqrt{3}(r_b + R_o)] \quad (3)$$

where m denotes the ionic radius corresponding to the subscript, and R_o denotes the oxygen ionic radius. The oxygen positional parameter u derived from Eq. (4) [50] exhibits a slight decreasing trend with increasing Ni substitution, as depicted in Fig. 5(c). This reduction suggests a subtle displacement of O^{2-} toward the A interstices, which facilitates the migration of Fe^{3+} ions from B to A sites. Such a structural adjustment provides further support for the cation redistribution mechanism driven by Ni substitution (Eq. (4)):

$$u = \frac{1}{\sqrt{3}a_{th}}(r_a + R_o) + \frac{1}{4} \quad (4)$$

Superexchange interactions, which govern magnetic ordering in spinel ferrites, are highly sensitive to the geometry of cation–oxygen–cation bonds [55]. According to the Goodenough–Kanamori–Anderson (GKA) rules [56], the strength of superexchange increases with shorter bond lengths and bond angles approaching 180°. As shown in Figs. 5(d)–5(f) and Table S7 in the ESM, the incorporation of Ni^{2+} leads to an increase in the A–B (θ_1, θ_2) and A–A (θ_5) bond angles, thereby enhancing the corresponding superexchange interactions. In contrast, the B–B bond angles (θ_3, θ_4) exhibit a slight reduction, indicating a weakening of B–B superexchange pathways. Table S7 in the ESM presents the theoretical interionic distances in MnZn ferrite (cation–anion distances: p, q, r, s; cation–cation distances: b, c, d, e, f) along with bond angles obtained from XRD Rietveld refinement. These observations suggest that Ni^{2+} substitution reconfigures the magnetic sublattices, enhancing A–B and A–A interactions at the expense of B–B coupling. From an electronic structure perspective, Ni^{2+} ($3d^8$) exhibits stronger orbital overlap with O^{2-} 2p orbitals than Mn^{2+} ($3d^5$), thereby facilitating a more efficient Ni^{2+}–O^{2-}–Fe^{3+} superexchange pathway. Additionally, the incorporation of Ni^{2+} causes a slight lattice contraction, which brings the Mn^{2+}–O–Fe^{3+} bond angle closer to the ideal 180°. Meanwhile, the bond lengths q and r, which characterize the strength of the superexchange interaction, gradually decrease, further enhancing the superexchange efficiency. These combined structural and electronic effects increase magnetic stiffness, suppress thermal spin fluctuations, and lead to the experimentally observed increase in T_c.

3.3 Magnetic and electrical properties

At 25 °C, as shown in Fig. 5(a), μ_i exhibits an initial increase followed by a decrease with increasing Ni substitution, reaching a maximum of 11,648 at x = 2. This behavior indicates that tmoderate Ni incorporation effectively reduces the magnetization

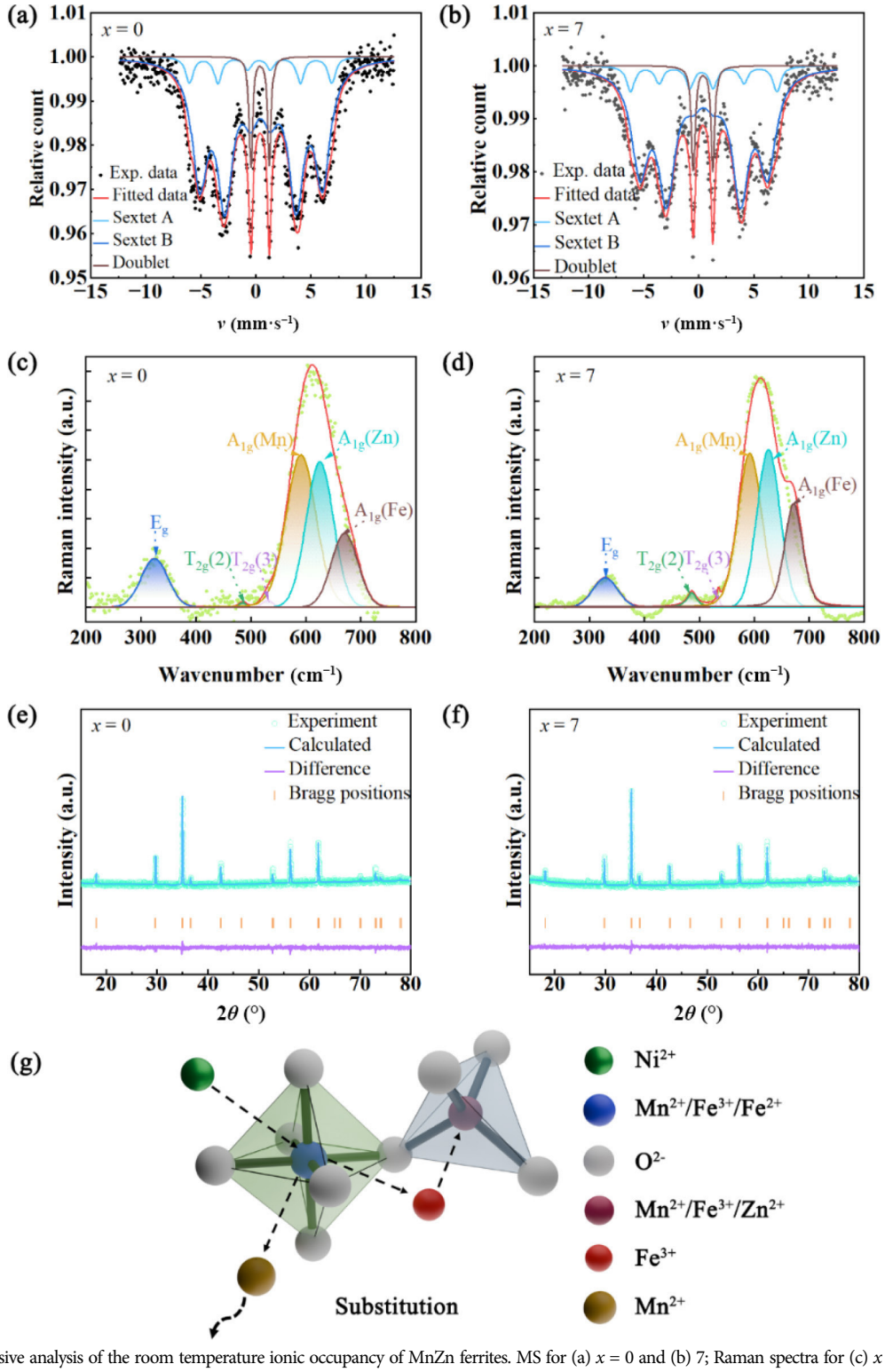

Fig. 4 Comprehensive analysis of the room temperature ionic occupancy of MnZn ferrites. MS for (a) $x = 0$ and (b) 7; Raman spectra for (c) $x = 0$ and (d) 7; XRD Rietveld refinement for (e) $x = 0$ and (f) 7; (g) lattice structure and cation substitution diagram.

resistance and enhances the magnetic susceptibility. As revealed in Fig. 3, minor segregation of Ni at the grain boundaries plays a decisive role in modifying the magnetization process of MnZn ferrites. The localized enrichment of Ni^{2+} enhances the magnetic exchange coupling across neighboring grains, thereby facilitating the formation of cross-grain magnetic domains. This transgranular domain continuity lowers the energy barrier for domain-wall motion, facilitates magnetization, and consequently yields higher μ_i.

When the Ni content exceeds the optimal level ($x > 2$), the chemical potential difference between the grain boundaries and grain interiors gradually diminishes, resulting in a more homogeneous distribution of Ni. This uniformity weakens local magnetic exchange coupling and suppresses transgranular domain formation. Simultaneously, the uniform substitution of Ni^{2+} ions increases lattice distortion and enhances magnetic anisotropy, both of which elevate domain-wall pinning energy and magnetic resistance. Consequently, μ_i decreases at higher Ni contents. These

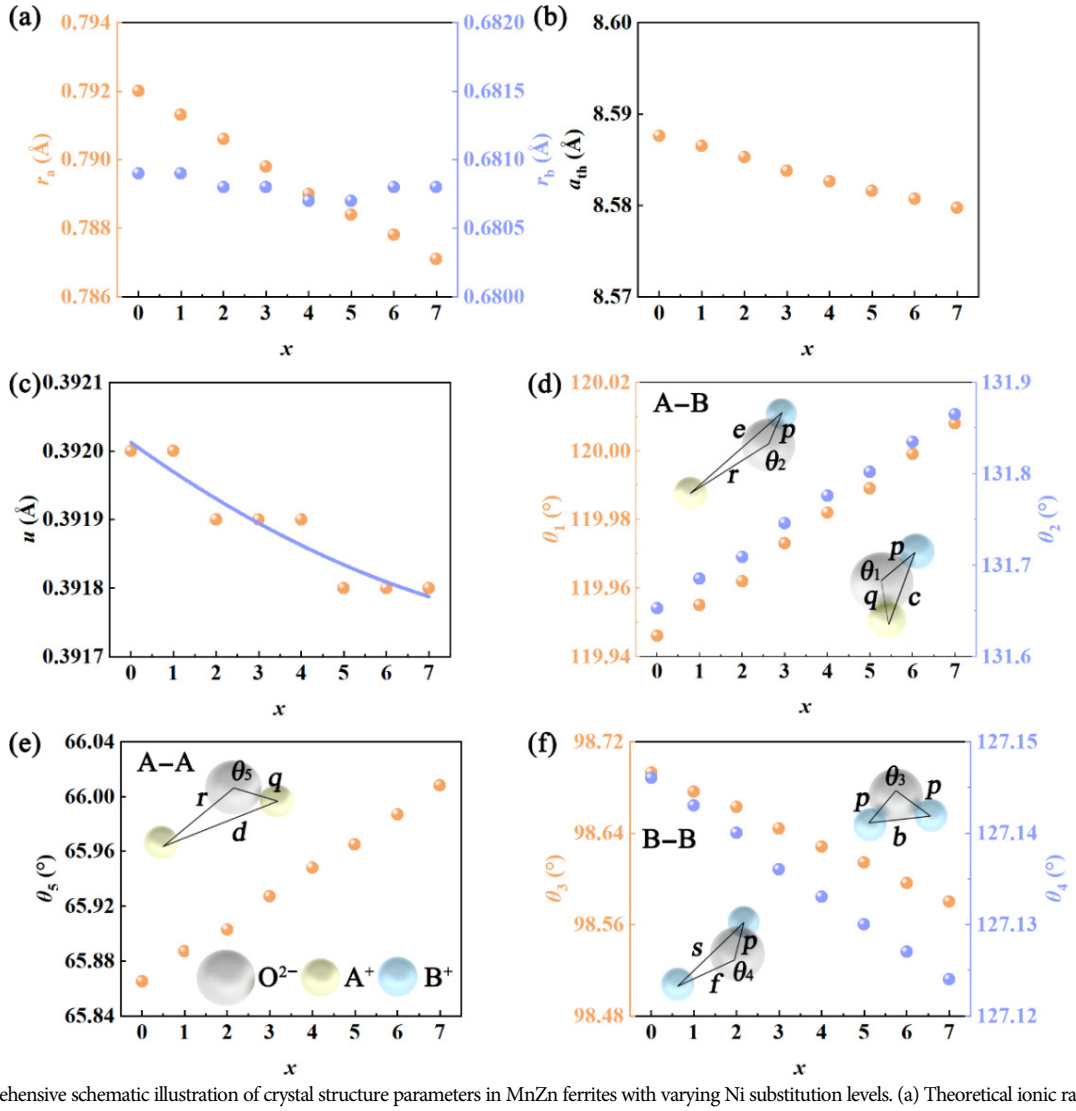

Fig. 5 Comprehensive schematic illustration of crystal structure parameters in MnZn ferrites with varying Ni substitution levels. (a) Theoretical ionic radii of cations at A and B sites, (b) theoretical lattice constants, (c) oxygen positional parameters in spinel structure, (d) superexchange angles θ_1 and θ_2 for A–B interactions, (e) superexchange angle θ_5 for A–A interactions, and (f) superexchange angles θ_3 and θ_4 for B–B interactions.

findings underscore the crucial influence of spatial Ni distribution in governing the magnetization behavior and μ_i of MnZn ferrites.

As shown in Fig. 6(b), the resistivity exhibits a nonlinear dependence on the Ni^{2+} content. Specifically, it first increases and then decreases as the Ni substitution level rises. This trend reflects the interplay between charge-carrier concentration and microstructural evolution induced by Ni incorporation. According to semiconductor theory, the resistivity of ferrites can be expressed as Eq. (5):

$$\rho = \frac{1}{nq\mu_n} \tag{5}$$

where n is the carrier concentration, q is the charge of the electron, and μ_n is the carrier mobility. MnZn ferrites are generally n-type semiconductors, in which electron hopping between Fe^{2+} and Fe^{3+} ions dominates charge transport. When Ni^{2+} occupies B sites in the spinel lattice, it introduces interstitial voids and modifies the local electronic environment, reducing the effective carrier concentration and thus increasing resistivity. Moreover, Ni substitution has been reported to raise the activation energy of electron hopping [57], further suppressing conduction. However, at higher levels of Ni^{2+} incorporation, excessive Ni^{2+} hinders grain growth and limits boundary phase development. The resulting thinner and less resistive grain boundaries facilitate charge transport, leading to the observed decline in resistivity at large substitution ratios.

Because the measured Z strongly depends on the sample geometry and coil configuration, the standardized impedance Z_0 was used to eliminate extrinsic effects. It is calculated by

$$Z_0 = Z \times \frac{L_e}{A_e} \times \frac{1}{N^2} \tag{6}$$

where L_e is the effective magnetic path length of the core, A_e is the effective cross-sectional area, and N is the number of coil turns. The frequency dependence of Z_0 for MnZn ferrites is shown in Fig. 6(c). As the Ni substitution increases, the peak frequency of Z_0 gradually shifts toward higher frequencies, while its magnitude slightly decreases. This behavior reflects the joint influence of the real and imaginary components of the complex μ_i, as well as the resistivity. The total Z can be expressed as Eq. (7):

$$|Z| = \sqrt{R^2 + X^2} = 2\pi f \mu_0 N^2 A_e / L_e \sqrt{\mu'^2 + \mu''^2} \tag{7}$$

where R is the real part of the Z (resistance), X is the imaginary part (reactance), f is the frequency, μ_0 is the vacuum μ_i, and μ' and

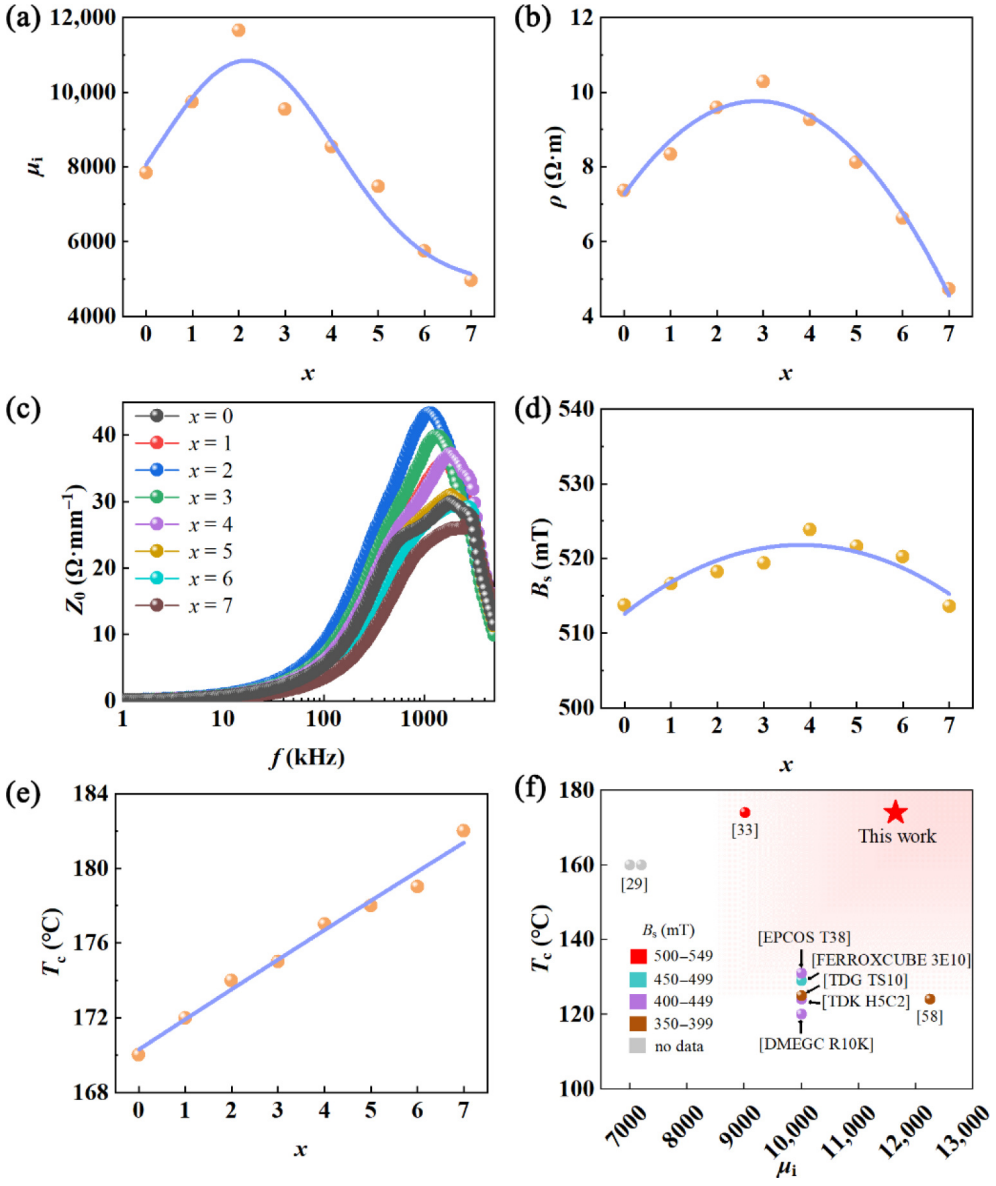

Fig. 6 Magnetic and electrical properties of $Mn_{0.5548-0.0056x}Zn_{0.3732}Ni_{0.0056x}Fe_{2.072}O_4$ ferrites with different Ni substitution levels. (a) μ_i for 25 °C, (b) resistivity, (c) frequency characteristics of Z_0, (d) B_s, (e) T_c, and (f) comparison of comprehensive performance with reported literature and commercial products.

μ'' are the real and imaginary components of the complex μ_i, respectively. The cutoff frequency (f_r), which corresponds to the Z_0 peak, is inversely proportional to μ_i. Hence, the Z_0 peak shifts toward higher frequencies as μ_i decreases. The optimal composition ($x = 2$) achieves the highest Z_0 value of 43 Ω·mm^{-1} at 1 MHz, whereas all samples exhibit 25 Ω·mm^{-1} and peak frequencies extending up to 3 MHz, indicating their suitability for high-frequency EMI suppression applications.

The variation in B_s with Ni content is shown in Fig. 6(d). B_s increases initially, reaching a maximum of 524 mT at $x = 4$, followed by a gradual decline. This nonmonotonic behavior originates from competing effects between cation redistribution and intrinsic magnetic moments. At lower substitution levels ($x \leq 4$), Ni^{2+} preferentially occupies B sites, displacing Fe^{3+} to A sites and enhancing densification (Table S8 in the ESM), thereby enhancing net magnetization. As the Ni content further increases, the replacement of high-spin Mn^{2+} ($3d^5$) by lower-moment Ni^{2+} ($3d^8$) reduces the total magnetic moment per formula unit. The overall magnetic moment μ_{total} can be expressed as Eq. (8):

$$\mu_{total} = \sum_i n_{Bi}\mu_{Bi} - \sum_j n_{Aj}\mu_{Aj} \quad (8)$$

where n_{Bi} and n_{Aj} represent the number of cations at the B and A sites, respectively, and μ_{Bi} and μ_{Aj} are their individual magnetic moments. At higher Ni substitution levels, the intrinsic reduction in magnetic moment, primarily due to the replacement of high-spin Mn^{2+} by lower-moment Ni^{2+}, surpasses the positive contribution from increased densification. This imbalance results in a net decrease in B_s. This emphasizes the delicate balance among cation distribution, magnetic moment, and microstructure in determining the magnetic performance of spinel ferrites.

Figure S8 in the ESM displays the temperature dependence of μ_i of $Mn_{0.5548-0.0056x}Zn_{0.3732}Ni_{0.0056x}Fe_{2.072}O_4$ ferrites. The T_c was extracted from this plot as the temperature corresponding to the x-axis intercept of the line connecting the data points representing 80% and 20% of the peak μ_i value. As shown in Fig. 6(e), the monotonic increase in T_c further corroborates the structural analysis in Section 3.2, confirming that Ni substitution strengthens A–B and A–A exchange interactions within the spinel lattice.

The optimized composition (x = 2) was compared with commercial ferrites and reported high-performance MnZn systems [29,33,58], as summarized in Fig. 6(f) and Table S9 in the ESM. Owing to the spatially engineered Ni distribution and enhanced intergranular exchange, the present ferrites exhibit superior comprehensive performance featuring high μ_i, large B_s, high T_c, and elevated Z within the kHz–MHz range, surpassing the properties of conventional and commercial MnZn ferrites.

4 Conclusions

Ni-substituted MnZn ferrites with a deliberately engineered nonuniform Ni distribution were successfully synthesized via conventional oxide ceramic processing. The resulting materials demonstrated excellent properties, including μ_i (11,648, at 10 kHz), Z_0 (43 Ω·mm^{-1}, at 1 MHz), B_s (524 mT, at 1 kHz, 1194 A·m^{-1}), and T_c (174 °C). The observed nonuniform Ni distribution significantly enhances intergranular exchange coupling, which facilitates the formation and propagation of magnetic domains across grain boundaries. This phenomenon enhances both μ_i and Z_0 of the MnZn ferrite. A higher magnetic moment density results in a higher B_s. Moreover, the superexchange interaction parameters θ_1, θ_2, and θ_5 associated with A–B- and A–A-type interactions increase with increasing Ni substitution, while the corresponding bond lengths decrease, indicating a progressive strengthening of both A–B and A–A superexchange interactions. This enhancement is closely associated with the observed upward shift in T_c. Collectively, these findings provide new insights into the design of MnZn ferrites with optimized magnetic and electrical performance and offer promising strategies for advancing the functionality of soft magnetic materials in high-frequency electronic devices.

Acknowledgements

This work was financially supported by the Regional Joint Fund of the National Natural Science Foundation of China (No. U25A20244), the National Natural Science Foundation (Nos. 52402332 and 52372255), the Science and Technology Department of Sichuan Province (Nos. 2024NSFSC0999 and 2024ZHCG0135), and the Central Guidance on Local Science and Technology Development Fund-Science and Technology Achievement Transformation Project (No. 2025ZYDF023).

Availability of data and materials

The data that support the findings of this study are available from the corresponding author upon reasonable request.

Competing interests

The authors have no competing interests to declare that are relevant to the content of this article.

Electronic Supplementary Material

Supplementary material is available in the online version of this article at https://doi.org/10.26599/JAC.2026.9221240.

References

[1] Liu YJ, He GQ, Zhang WJ, *et al.* Low loss and temperature-stable $Y_3MgAl_3GeO_{12}$ microwave dielectric ceramics for X-band applications. *J Adv Ceram* 2025, **14**: 9221136.
[2] Qiu SH, Zou J, Liu JJ, *et al.* Superhard B_4C-based composites with multifunctionality. *Acta Mater* 2025, **288**: 120817.
[3] Blaž NV, Luković MD, Nikolic MV, *et al.* Heterotube Mn–Zn ferrite bundle EMI suppressor with different magnetic coupling configurations. *IEEE T Magn* 2014, **50**: 8000907.
[4] Wei W, Huang M, Yao WL, *et al.* Circulating current suppression for ground tied variable frequency to constant frequency converter system in aircraft. *Chinese J Aeronaut* 2023, **36**: 386–397.
[5] Mandal D, Bhandari B, Mullurkara SV, *et al.* All-around electromagnetic wave absorber based on Ni–Zn ferrite. *ACS Appl Mater Inter* 2024, **16**: 33846–33854.
[6] Kruželák J, Kvasničáková A, Hložeková K, *et al.* Electromagnetic interference shielding and physical-mechanical characteristics of rubber composites filled with manganese–zinc ferrite and carbon black. *Polymers-Basel* 2021, **13**: 616.
[7] Suarez A, Victoria J, Torres J, *et al.* Performance study of split ferrite cores designed for EMI suppression on cables. *Electronics* 2020, **9**: 1992.
[8] Li Y, Zhang ZH, Yu JY, *et al.* High-frequency modeling and analysis of single-layer NiZn ferrite inductors for EMI filtering in power electronics applications. *Energies* 2024, **17**: 5657.
[9] Kącki M, Ryłko MS, Hayes JG, *et al.* Measurement methods for high-frequency characterizations of permeability, permittivity, and core loss of Mn–Zn ferrite cores. *IEEE T Power Electr* 2022, **37**: 15152–15162.
[10] Thakur P, Chahar D, Taneja S, *et al.* A review on MnZn ferrites: Synthesis, characterization and applications. *Ceram Int* 2020, **46**: 15740–15763.
[11] Chen ZX, Li T, Wang AP, *et al.* The latest research progress on MnZn ferrite and their applications. *Open Ceram* 2025, **21**: 100732.
[12] Luo F, Duan ZX, Zhang YY, *et al.* Influence of microstructure optimization on magnetic and thermal properties of MnZn ferrite. *J Mater Sci-Mater El* 2021, **32**: 15633–15642.
[13] Yu Z, Lan ZW, Wang JM, *et al.* Effect of additives on magnetic properties of high frequency MnZn power ferrite. *J Ele Sci Technol* 2004, **2**: 22–25.
[14] Martinson KD, Panteleev IB, Steshenko KA, *et al.* Effect of Bi_2O_3 contents on magnetic and electromagnetic properties of LiZnMn ferrite ceramics. *J Eur Ceram Soc* 2022, **42**: 3463–3472.
[15] Yi SB, Bai GH, Wang XY, *et al.* Development of high-temperature high-permeability MnZn power ferrites for MHz application by Nb_2O_5 and TiO_2 co-doping. *Ceram Int* 2020, **46**: 8935–8941.
[16] Wu GH, Yu Z, Tang ZD, *et al.* Effect of $CaCO_3$ and V_2O_5 composite additives on the microstructure and magnetic property of MnZn ferrites. *IEEE T Magn* 2018, **54**: 6300707.
[17] Li QF, Liu XY, Wang H, *et al.* Grain-boundary-engineered MnZn ferrites with suppressed power loss and enhanced temperature stability. *Ceram Int* 2025, **51**: 20813–20821.
[18] Ying Y, Gong YZ, Liu D, *et al.* Effect of MoO_3 addition on the magnetic properties and complex impedance of Mn–Zn ferrites with high B_s and high initial permeability. *J Supercond Nov Magn* 2017, **30**: 2129–2134.
[19] Ahmad M, Asif MI, Drissi N, *et al.* Influence of La-substitution and SiO_2 additives on structure, magnetic and high frequency dielectric properties of Co_2W hexagonal ferrites synthesized by sol–gel auto-combustion method. *J Inorg Organomet P* 2025, **35**: 4368–4382.
[20] Singh AP, Pandey OP, Sharma P. Impedance spectroscopy and magnetic studies on Co_2Z ferrite sintered with SiO_2 and Bi_2O_3 additives. *Mater Chem Phys* 2022, **277**: 125574.
[21] Ying Y, Feng JW, Li ZC, *et al.* Effect of a YIG nanoparticle additive on the magnetic properties of MnZn ferrites for MHz frequency applications. *J Am Ceram Soc* 2023, **106**: 251–258.
[22] Wu GH, Yu Z, Sun K, *et al.* Ultra-low core losses at high frequencies and temperatures in MnZn ferrites with nano-$BaTiO_3$ additives. *J Alloys Compd* 2020, **821**: 153573.
[23] Cantwell PR, Tang M, Dillon SJ, *et al.* Grain boundary complexions. *Acta Mater* 2014, **62**: 1–48.
[24] Andalib P, Chen YJ, Harris VG. Concurrent core loss suppression and high permeability by introduction of highly insulating intergranular magnetic inclusions to MnZn ferrite. *IEEE Magn Lett* 2018, **9**: 5100705.
[25] Töpfer J, Angermann A. Complex additive systems for Mn–Zn ferrites with low power loss. *J Appl Phys* 2015, **117**: 17A504.

[26] Li ZY, Jin HY, Wang H, *et al.* Microstructure, magnetic properties, and loss performance of the Cu-substituted MnZn ferrites. *Ceram Int* 2023, **49**: 40275–40283.
[27] Yang P, Liu ZQ, Qi HB, *et al.* Significantly improved near-field communication antennas based on novel Ho^{3+} and Co^{2+} ions Co-doped Ni–Zn ferrites. *J Adv Ceram* 2024, **13**: 293–309.
[28] Zhang XF, Li QF, Wu T, *et al.* Site-controlled multi-ion substitution enabling low-loss and high-permittivity microwave ferrites. *J Adv Ceram* 2025, **14**: 9221076.
[29] Ying Y, Zheng HH, Li ZC, *et al.* Substitution of Sn in the high-permeability MnZn ferrite for wide temperature applications. *Ceram Int* 2024, **50**: 29914–29919.
[30] Zhang HY, Li QF, Jiang XN, *et al.* Power capacity enhancement and loss reduction induced by limited solid solubility of Ho^{3+} rare-earth substitution in NiCuZn spinel ferrites. *J Adv Ceram* 2024, **13**: 1655–1665.
[31] Wu GH, Yu Z, Guo RD, *et al.* Effects of Sn substitution on the microstructural and electromagnetic properties of MnZn ferrite for high-frequency applications. *J Phys D Appl Phys* 2023, **56**(18): 185001.
[32] Zeng X, Hou ZP, Ju JQ, *et al.* The cation distributions of Zn-doped normal spinel $MgFe_2O_4$ ferrite and its magnetic properties. *Materials* 2022, **15**: 2422.
[33] Wu T, Wang C, Li ZY, *et al.* A comprehensive study on MnZn ferrite materials with high saturation magnetic induction intensity and high permeability for magnetic field energy harvesting. *J Magn Magn Mater* 2024, **590**: 171635.
[34] Li QF, Ni HN, Wu CJ, *et al.* Vacancy-engineered Gd^{3+}-substituted yttrium iron garnet with narrow ferrimagnetic linewidth and high Curie temperature. *J Alloys Compd* 2023, **935**: 168169.
[35] Zipare KV, Bandgar SS, Shahane GS. Effect of Dy-substitution on structural and magnetic properties of MnZn ferrite nanoparticles. *J Rare Earth* 2018, **36**: 86–94.
[36] Jeong WH, Han YH. Power losses of Ni-substituted Mn–Zn ferrites. *Jpn J Appl Phys* 2003, **42**: 1233–1236.
[37] Ahmed FA, Singh LN. Effect of Ni substitution on structural and magnetic properties of Mn-Zn ferrite nanoparticles. *J Mate Sci Surf Eng* 2018, **6**: 825–830.
[38] Fan XY, Bai GH, Zhang ZH, *et al.* Correlating the microstructure with magnetic properties of Ti-doped high-frequency MnZn ferrite. *J Eur Ceram Soc* 2023, **43**: 5540–5547.
[39] Yan M, Yi SB, Fan XY, *et al.* High-frequency MnZn soft magnetic ferrite by engineering grain boundaries with multiple-ion doping. *J Mater Sci Technol* 2021, **79**: 165–170.
[40] Kogias G, Zaspalis S, Holz D, *et al.* The effect of Ni on the magnetic properties of power or high permeability MnZn ferrites. *J Magn Magn Mater* 2024, **604**: 172297.
[41] Varshney D, Yogi A. Structural, vibrational and magnetic properties of Ti substituted bulk hematite: α-$Fe_{2-x}Ti_xO_3$. *J Adv Ceram* 2014, **3**: 269–277.
[42] Mehmood R, Fan WJ, Hu X, *et al.* Confirming high-valent iron as highly active species of water oxidation on the Fe, V-coupled bimetallic electrocatalyst: *In situ* analysis of X-ray absorption and mössbauer spectroscopy. *J Am Chem Soc* 2023, **145**: 12206–12213.
[43] De Coster V, Srinath NV, Theofanidis SA, *et al.* Looking inside a Ni–Fe/$MgAl_2O_4$ catalyst for methane dry reforming *via* Mössbauer spectroscopy and *in situ* QXAS. *Appl Catal B-Environ* 2022, **300**: 120720.
[44] Sandim MJR, Nagamine LCCM, da Silva AK, *et al.* Anomalous magnetization induced by local chemistry fluctuations in Mn-containing α'-martensite. *Acta Mater* 2024, **272**: 119956.
[45] Msomi JZ, Moyo T, Dolo JJ. Heat treatment effects on spinel phase of $Zn_xNi_{1-x}Fe_2O_4$ and $MnFe_2O_4$ nanoferrites. *Hyperfine Interact* 2010, **197**: 59–64.
[46] Arana M, Galván V, Jacobo SE, *et al.* Cation distribution and magnetic properties of LiMnZn ferrites. *J Alloys Compd* 2013, **568**: 5–10.
[47] Cuscó R, Taguchi A, Yamaguchi T. Phonon anharmonicity in α-In_2O_3: A Raman scattering study of the A1 modes. *J Alloys Compd* 2025, **1020**: 179350.
[48] Song YJ, Cui YP, Geng L, *et al.* Li/Ni intermixing: The real origin of lattice oxygen stability in co-free Ni-rich cathode materials. *Adv Energy Mater* 2024, **14**: 2303207.
[49] Sun K, Wu CJ, Yang Y, *et al.* Cation distribution and temperature dependence of Brillouin function for nickel-substituted manganese–zinc ferrites. *IEEE T Magn* 2015, **51**: 6301304.
[50] Sharma R, Thakur P, Kumar M, *et al.* Improvement in magnetic behaviour of cobalt doped magnesium zinc nano-ferrites *via* co-precipitation route. *J Alloys Compd* 2016, **684**: 569–581.
[51] Venkataraju C, Sathishkumar G, Sivakumar K. Effect of cation distribution on the structural and magnetic properties of nickel substituted nanosized Mn–Zn ferrites prepared by co-precipitation method. *J Magn Magn Mater* 2010, **322**: 230–233.
[52] Cho Y, Oh P, Cho J. A new type of protective surface layer for high-capacity Ni-based cathode materials: Nanoscaled surface pillaring layer. *Nano Lett* 2013, **13**: 1145–1152.
[53] Bhukal S, Dhiman M, Bansal S, *et al.* Substituted Co–Cu–Zn nanoferrites: Synthesis, fundamental and redox catalytic properties for the degradation of methyl orange. *RSC Adv* 2016, **6**: 1360–1375.
[54] Remsungnen T, Rode BM. Molecular dynamics simulation of the hydration of transition metal ions: The role of non-additive effects in the hydration shells of Fe^{2+} and Fe^{3+} ions. *Chem Phys Lett* 2004, **385**: 491–497.
[55] Kumar G, Shah J, Kotnala RK, *et al.* Superparamagnetic behaviour and evidence of weakening in super-exchange interactions with the substitution of Gd^{3+} ions in the Mg–Mn nanoferrite matrix. *Mater Res Bull* 2015, **63**: 216–225.
[56] Yin LH, Zhao GC, Tong P, *et al.* Control of magnetism at low electric fields in multiferroic $0.58BiFeO_3$–$0.42Bi_{0.5}K_{0.5}TiO_3$ single crystal near morphotropic phase boundary. *Acta Mater* 2023, **255**: 119044.
[57] Gawas UB, Verenkar VMS, Vader VT, *et al.* Effects of sintering temperature on microstructure, initial permeability and electric behaviour of Ni–Mn–Zn ferrites. *Mater Chem Phys* 2022, **275**: 125250.
[58] Jiang KQ, Li KK, Peng CH, *et al.* Effect of multi-additives on the microstructure and magnetic properties of high permeability Mn–Zn ferrite. *J Alloys Compd* 2012, **541**: 472–476.